Magnetism and the spin state in cubic perovskite $CaCoO_3$ synthesized under high pressure

Hailiang Xia,[1,2] Jianhong Dai,[1,2] Yuanji Xu,[1,2] Yunyu Yin,[1,2] Xiao Wang,[1,2] Zhehong Liu,[1,2] Min Liu,[1] Michael A. McGuire,[3] Xiang Li,[4] Zongyao Li,[4] Changqing Jin,[1,2,5] Yifeng Yang,[1,2,5] Jianshi Zhou,[4,*] and Youwen Long[1,2,5,†]

[1]*Beijng National Laboratory for Condensed Matter Physics, Institute of Physics, Chinese Academy of Sciences, Beijing 100190, China*

[2]*School of Physical Sciences, University of Chinese Academy of Sciences, Beijing 100190, China*

[3]*Materials Science and Technology Division, Oak Ridge National Laboratory, Oak Ridge, Tennessee 37831, USA*

[4]*Materials Science and Engineering Program, Department of Mechanical Engineering, University of Texas, Austin, Texas 78712, USA*

[5]*Collaborative Innovation Center of Quantum Matter, Beijing 100190, China*

(Received 1 April 2017; published 17 July 2017)

Cubic $SrCoO_3$ with an intermediate spin state can only be stabilized by high pressure and high temperature (HPHT) treatment. It is metallic and ferromagnetic with the highest Curie temperature of the transition-metal perovskites. The chemical substitution by Ca on Sr sites would normally lower crystal symmetry from cubic to orthorhombic as seen in the perovskite family of $CaMO_3$ ($M = M^{4+}$ of transition metals, Ge^{4+}, Sn^{4+}, and Zr^{4+}) at room temperature. This structural change narrows the bandwidth, so as to further enhance the Curie temperature as the crossover to the localized electronic state is approached. We report a successful synthesis of the perovskite $CaCoO_3$ with a HPHT treatment. Surprisingly, $CaCoO_3$ crystallizes in a simple cubic structure that remains stable down to 20 K, the lowest temperature in the structural study. The new perovskite has been thoroughly characterized by a suite of measurements including transport, magnetization, specific heat, thermal conductivity, and thermoelectric power. Metallic $CaCoO_3$ undergoes two successive magnetic transitions at 86 K and 54 K as temperature decreases. The magnetization at 5 K is compatible with the intermediate spin state t^4e^1 of Co^{4+} at the octahedral site. The thermal expansion of the Co-O bond length indicates that the population of high spin state t^3e^2 increases for $T > 100$ K. The shortest Co-O bond length in cubic $CaCoO_3$ is responsible for delocalizing electrons in the π^*-band and itinerant-electron ferromagnetism at $T < 54$ K. A comprehensive comparison between $SrCoO_3$ and $CaCoO_3$ and the justification of their physical properties by first-principles calculation have also been made in this report. Partially filled π^* and σ^* bands would make $CaCoO_3$ suitable to study the Hund's coupling effect in a metal.

DOI: 10.1103/PhysRevMaterials.1.024406

I. INTRODUCTION

Perovskite cobalt oxides have been well known for a spin-state transition due to the exchange splitting Δ_{ex} matching the crystal-field splitting energy Δ_c. For Co^{3+} in $RCoO_3$ (R = rare earth), depending on the bandwidth W of the σ^* band and $\Delta = \Delta_{ex} - \Delta_c$, the perovskites can exhibit the low-spin (LS) state t^6e^0 and higher-spin (HS) state $t^{6-x}e^x$ [1–5]. The spin state transition can be tuned either by a chemical substitution of the rare earth [6] or varying temperature, as in the thermally driven spin-state transition found in $LaCoO_3$ [7]. It appears for the perovskites with Co^{4+} that a $\Delta = \Delta_{ex} - \Delta_c \approx 0$ holds also, which led Potze *et al.* [8] to propose the intermediate-spin (IS) state $t_2^4e^1$ in order to explain the x-ray absorption spectra in $SrCoO_3$. The IS state has been shown to be consistent with the magnetization measurement of a single-crystal sample of $SrCoO_3$ [9]. The spin state transition is normally associated with anomalies of transport and magnetic properties [10,11], thermal expansion [12–14], bulk modulus [15,16], and the inelastic property [17]. In addition to the interest of fundament research on the spin-state transition, the capability to manipulate the spin state in transition-metal oxides can also be used to enhance catalytic properties for clean-energy technology [18].

In a cubic crystal field, the σ^* band of transition-metal oxides is broader than the π^* band. Populating electrons in the σ^* band normally leads an increase in the conductivity. Electrons in the σ^* band can also undergo a localized to itinerant transition. In the $RNiO_3$ family, an evolution from a localized to an itinerant electronic state can be tuned through either chemical substitution [19–21] or by applying hydrostatic pressure [22–24] on a composition on the localized-electron side of the transition. At ambient pressure, the bond length mismatch between the R-O and Ni-O bonds progressively lowers the crystal symmetry from rhombohedral to orthorhombic depending on the ionic radii of R^{3+}. As a result, the Ni-O-Ni bond angle is reduced from 180° by an angle θ in the phases with lower symmetries. The width of the σ^* band is related to $\cos\theta$ [24]. On crossing the insulator-metal transition, the Ni-O bond length changes abruptly [25], indicating a first-order transition. The electron-electron correlations facilitate the spin-spin exchange interaction. For localized electrons, the perturbation formula of superexchange interaction $T_N \sim J \sim b^2/U$ applies, where U is the on-site correlation energy and b is the orbital overlap integral. On the itinerant-electron side, any magnetic transition gradually fades away as the bandwidth broadens. The magnetic transition temperature peaks at the crossover as predicted by solving the Mott-Hubbard Hamiltonian numerically [26]. This scenario has been applied to explain an enormously high T_N found in $SrTcO_3$ and $CaTcO_3$ [27–29].

Compared to Co(III) in $RCoO_3$, Co(IV) in $ACoO_3$ (A = alkaline earth) has a much enhanced d-p hybridization because

*Corresponding author: jszhou@mail.utexas.edu

†Corresponding author: ywlong@iphy.ac.cn

 ©2017 American Physical Society

the $Co^{3+/4+}$ redox potential moves to the top of the O $2p$ band, which leads to a broadening of the σ^* band. The metallic $SrCoO_3$ with the IS state is consistent with a broader σ^* band [9,30]. The ferromagnetism found in the metallic $SrCoO_3$, however, is likely caused by the direct exchange interaction in the system with itinerant electrons in the σ^* band and localized electrons on the t_2 orbitals. A further reduction of the Co-O bond in the cobalt oxide may lead to either the IS to LS transition or delocalizing the t_2 electrons. In this paper, we report the successful synthesis of $CaCoO_3$ for the first time. In contrast to the normal relationship between the crystal structure and the chemical substitution in perovskite oxides, the Ca substitution does not lead to a transition from the cubic to the orthorhombic structure. Instead, $CaCoO_3$ remains in the cubic phase. $CaCoO_3$ not only stands out in terms of the crystal structure among $CaMO_3$ perovskites ($M = M^{4+}$ of transition metals, Ge^{4+}, Sn^{4+}, Zr^{4+}), but also shows physical properties rarely seen in transition-metal oxides.

$SrCoO_3$ crystallizes in the cubic perovskite structure with the Pm-$3m$ space group [9,30]. High oxygen pressure is needed to stabilize the Co^{4+} valance state. By using the structural prediction software SPuDs [31] for perovskite phases, a geometric tolerance factor $t \approx 1$ can be obtained for $CaCoO_3$, which means that a similar cubic phase should be stabilized in $CaCoO_3$. However, all attempts to synthesize $CaCoO_3$ failed so far. This difficulty has been overcome in this work by oxidizing the brownmillerite $Ca_2Co_2O_5$ under high oxygen pressure.

II. DETAILS ABOUT EXPERIMENTS AND THE CALCULATION

We have applied the two-step method used for the $SrFe_{1-x}Co_xO_3$ solid solution [32] to synthesize $CaCoO_3$. As the first step, oxygen-deficient $Ca_2Co_2O_5$ with the brownmillerite structure was prepared by following the procedure reported elsewhere [33]. Then a $Ca_2Co_2O_5$ pellet, 3.0 mm in diameter and 2.0 mm in length, was sealed into a Pt capsule together with the oxygen releasing agent $KClO_4$ at both ends of the precursor. The assembly, including the capsule, heater, and pressure medium, was treated at 7 GPa and 1500 K for half an hour in a cubic anvil-type high-pressure apparatus [34]. At the end of this high-pressure treatment, the heating power was shut down before the pressure was released. The high-pressure products were first checked by using powder x-ray diffraction (XRD) on a Huber diffractometer (Cu-Kα_1 radiation, 40 kV, 30 mA). The sample with a single phase of the perovskite structure was further studied with a PANalytical X'pert diffractometer (Cu-Kα_1 radiation) with an Oxford PheniX cryostat at Oak Ridge National Laboratory. Crystallographic parameters were obtained by using Rietveld refinement with the FULLPROF program [35]. Thermogravimetric (TG) analysis was performed on a Setaram TG-DTA system with a temperature scan up to 1200 K in a gas flow of the mixture H_2 (4%) and N_2 (96%). The temperature-dependent magnetization was measured by using a superconducting quantum interference device (SQUID) magnetometer from Quantum Design with the applied fields $H = 0.1$ and 1 T. The SQUID magnetometer and the VSM in a Physical Property Measurement System (PPMS) were used to perform the isothermal magnetization measurements. The data of electrical transport and specific heat were collected on the PPMS. Measurements of thermal conductivity and thermoelectric power were carried out with homemade setups. The structural study under high pressure was carried out by using a diamond anvil cell. The detailed information about the setup can be found in Ref. [16].

First-principles calculations were performed by using the full-potential augmented plane-wave and local orbital methods [36], as implemented in the WIEN2k code [37]. To include the strong correlations for electrons in $CaCoO_3$, we used the GGA-PBE [38] exchange-correlation functional with effective Coulomb repulsions (U_{eff}) in the GGA + U calculations. The muffin-tin radii were set to be 2.43 a.u. for Ca, 1.82 a.u. for Co, and 1.62 a.u. for O atoms; $R_{\text{MT}}K_{\text{max}} = 8.00$ and 3000 k-point meshes were used over the whole Brillouin zone. We also optimized the lattice parameter of $CaCoO_3$ and the obtained lattice parameter is in good agreement with the experiment results.

III. RESULTS

Figure 1(a) shows the powder XRD pattern of $CaCoO_3$ at room temperature. The structural model used to refine the profile is a simple Pm-$3m$ cubic perovskite with the lattice parameter $a = 3.73431(6)$ Å. The fitting goodness comes as a surprise since all existing $CaMO_3$ ($M = M^{4+}$ of transition metals, Ge^{4+}, Sn^{4+}, Zr^{4+}) adopt the $Pbnm$ orthorhombic structure at room temperature [39]. Refinements with other structural models of the perovskite tilting systems such as $a^0a^0c^+$ ($I4/mcm$) and $b^-a^+b^-$ ($Pbnm$) gave slightly worse results in terms of the reliable factor R. Moreover, the absence of the low-angle peaks such as the one near $2\theta \sim 25^\circ$ seems to rule out the possibility of having the $Pbnm$ structure. The $a^0a^0c^+$ tilting system does not produce the weak diffractions at low angles; but all these tilting systems have diffraction peaks split from that of the cubic phase at higher angles, which is clearly not matching to the narrow diffraction peaks observed. The TGA analysis in Fig. 1(b) gives a near oxygen stoichiometry (2.98 ± 0.02) of the sample. We have a good reason to fix the oxygen occupation in the refinement with the cubic model. The refinement with the cubic structural model is, however, not airtight. Since the atomic displacement parameter B is the only refining parameter in addition to the lattice parameter, a slightly higher intensity of the peak near 60° forces the program to yield an unusually high $B(\text{Å}^2) \sim 13$ for the oxygen; a similar B value has been found at 1000 °C in $CaTiO_3$ [40,41]. Whereas there is a high uncertainty about the B value from refining the x-ray diffraction pattern, a high B value may indicate oxygen fluctuations, which could be correlated to an unusually low thermal conductivity of the $CaCoO_3$ perovskite, which will be further discussed in a following paragraph. All structural parameters from the refinement are listed in Table I and more detailed information about the structural refinement is provided in the Supplemental Material [69].

Figure 2(a) shows the temperature dependence of the magnetization. Fitting the temperature dependence of paramagnetic susceptibility above 200 K to a Curie-Weiss law gives a $\mu_{\text{eff}} = 3.58\ \mu_B$, which is close to the spin-only value of the IS state $S = 3/2$ ($\mu_{\text{eff}} = 3.87\ \mu_B$). With decreasing

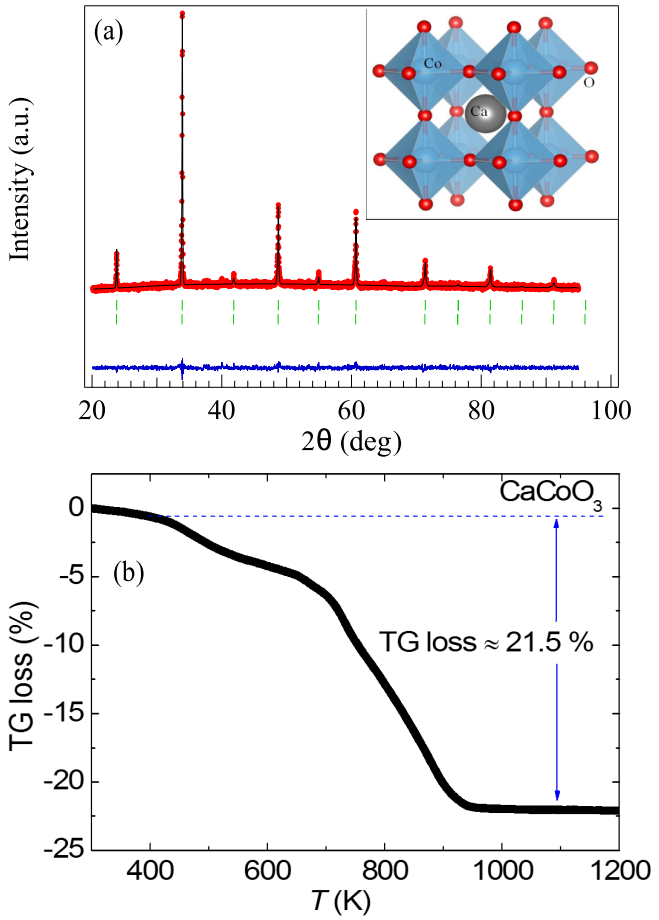

FIG. 1. (a) X-ray diffraction pattern and the result of Rietveld refinement with the cubic model for $CaCoO_3$; observed (circles), calculated (black line), and the difference (blue line) are shown in the patterns. The detailed information about the refinement is given in the Supplemental Material [69]. The inset is the structural model of a cubic perovskite. (b) Temperature dependence of thermogravimetric (TG) loss for $CaCoO_3$. The weight of $CaCoO_3$ slightly decreases for $T > 300$ K. This weight change can usually be attributed to the loss of the surface absorption, especially in the grain boundaries due to the usage of oxidizing agent added during the synthesis. Above 400 K, the TG loss starts to decrease quickly, suggesting the occurrence of decomposition reaction. According to the TG loss between 400 and 1200 K as well as the final products (CaO and Co), the oxygen content of $CaCoO_3$ can be determined to be 2.98 ± 0.02. This value is very close to the ideal chemical composition, confirming the formation of the Co^{4+} valance state in $CaCoO_3$.

TABLE I. Refinement structure parameters of $CaCoO_3$ obtained at room temperature. Space group: Pm-$3m$; Atomic positions: Ca (0.5, 0.5, 0.5), Co (0, 0, 0), O (0.5, 0, 0).

Parameter	
a (Å)	3.73431(6), 97% volume
	3.7391(2), 3% volume
R_{wp} (%)	3.59
R_p (%)	2.8
χ^2	1.4

temperature, an anomaly of $M(T)$ occurs at 86 K; it seems an AFM transition as seen from a zoomed-in plot of $M(T)$ in the inset. The AFM transition is followed by another magnetic transition at ~54 K as temperature further decreases. These magnetic transitions can also be confirmed by anomalies in the specific heat at the corresponding temperatures in Fig. 2(b). A dramatic increase of the magnetization on cooling through 55 K identifies this as a ferromagnetic transition. The downturn observed in the $M(T)$ data upon cooling below 25 K and the separation between the field-cooled and zero-field-cooled data may be attributed to an increase in magnetic anisotropy upon cooling, or it may indicate that the low-temperature magnetic structure is more complex than a simple collinear ferromagnet. Ferromagnetism below 54 K is further supported by the well-defined magnetic saturation and a small coercive field observed at $T < 54$ K in Fig. 2(c). A magnetic-field-induced transition is observed at temperatures below T_N as shown in Fig. 2(d) for $T = 70$ K. The onset field H_t to trigger the transition at 70 K is about 5.5 T, which increases slightly at lower temperatures. The saturation moment M_s shows a pronounced increase at H_t. While M_s continues to increase for $H > H_t$, it is still less than 1.0 μ_B at 14 T. In comparison, M_s is about 2.5 μ_B for $SrCoO_3$ [9].

The resistivity of $CaCoO_3$ in Fig. 2(e) is smaller than that of $SrCoO_3$ by one order in magnitude at room temperature and behaves metallic down to 2 K. An obvious drop of resistivity on cooling through T_c observed in $CaCoO_3$ is absent in $SrCoO_3$ [30], but is similar to the behavior of $\rho(T)$ on cooling through a ferromagnetic transition temperature T_c in metallic $SrRuO_3$ [42–44]. Whereas $SrCoO_3$ exhibits a small magnetoresistance (MR) at low temperatures [9], the MR effect is strongly enhanced and peaks around T_c in $CaCoO_3$ as shown in Fig. 2(f).

Figure 3 shows the detailed change of magnetization curves at different temperatures. Compared to the isotherm of $M(H)$ at $T > T_N$, the magnetic order induces a strong nonlinear behavior at low field and a metamagnetic transition at H_t which increases progressively as temperature decreases. The correlation between the field-induced change of the magnetization and the MR effect of resistivity at 40 K is shown in Fig. 4. At the magnetic field where the inflection point of the magnetization curve occurs, a decrease of resistivity is clearly visible.

In order to confirm an AF transition in $CaCoO_3$ on cooling through 86 K, we have measured the $C_p(T)$ under different magnetic fields. Figure 5 shows the $C_p(T)$ of $CaCoO_3$ in a narrow temperature range near 86 K. The λ-shape anomaly at 86 K is typical for a second-order magnetic transition. Magnetic field has no effect on $C_p(T)$ at $T > 90$ K, but the peak profile representing the entropy change associated with the magnetic ordering becomes broad with the peak position moving to lower temperatures under magnetic field, which is commonly seen for an AF transition.

The positive thermoelectric power S of $CaCoO_3$ shown in Fig. 6(a) appears not to be consistent with a less than 1/4-filled σ^* band in the HS ($t^{5-x}e^x$) state of $CaCoO_3$. The hybridization with a partially filled π^* band may be a factor for a positive thermoelectric power. The $S(T)$ of $SrCoO_3$ also given in Fig. 6(a) is positive at room temperature. In comparison with $SrCoO_3$, a much lower thermoelectric power value of $CaCoO_3$ at room temperature would indicate a broader bandwidth in

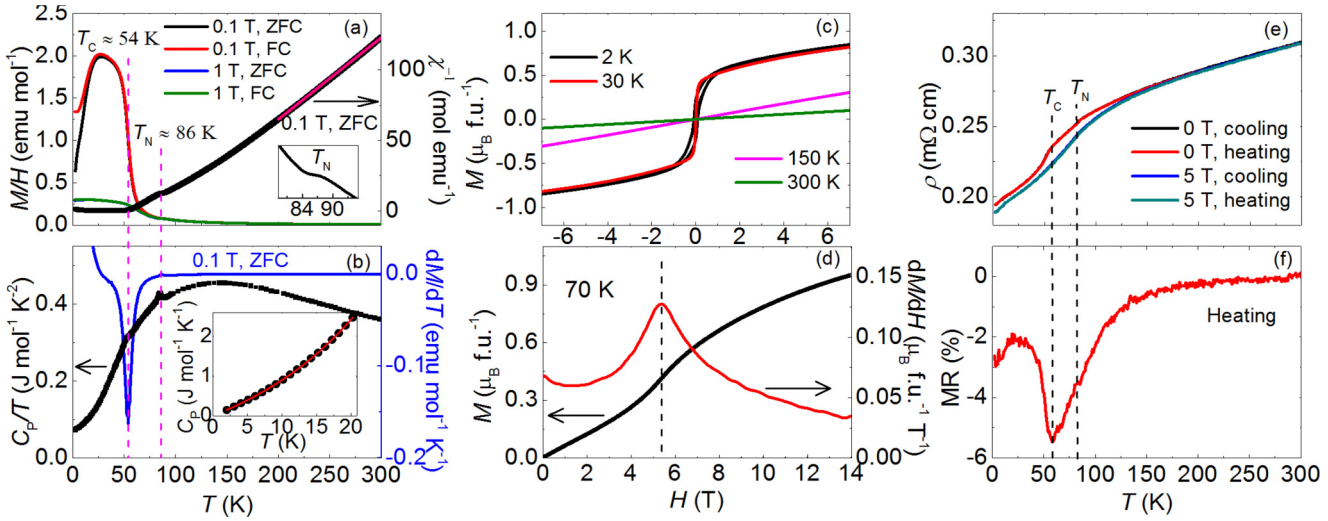

FIG. 2. Magnetic and transport properties of $CaCoO_3$. Temperature dependence of (a) magnetization in both zero-field cooling (ZFC) and field cooling (FC), and (b) specific heat. (c), (d) Field dependence of magnetization at different temperatures. Temperature dependence of (e) resistivity measured at zero field and 5 T, and (f) the magnetoresistance MR(%) $= 100\%[\rho(5\text{ T}) - \rho(0)]/\rho(0)$. The inset in (a) shows an enlarged view for the AFM transition. The red line in the inverse susceptibility in (a) shows the fit of $\chi^{-1}(T)$ to a Curie-Weiss law between 200 and 300 K. The derivative of magnetization in (b) is used to determine the magnetic phase transition temperatures. The red curve in the inset (b) shows the fit of specific heat to the formula $C_p = \gamma T + \beta T^{3/2} + \alpha T^3$, giving $\gamma = 66.3(2)\,\text{mJ mol}^{-1}\,\text{K}^{-2}$, $\beta = 4.8(6)\,\text{mJ mol}^{-1}\,\text{K}^{-5/2}$, and $\alpha = 0.083(3)\,\text{mJ mol}^{-1}\,\text{K}^{-4}$.

$CaCoO_3$ than that in $SrCoO_3$, which is also consistent with the comparison of resistivity in these two cobalt oxides. While S increases monotonically with increasing temperature, $S(T)$ does not fit the Mott diffusive model of the thermoelectric power for a metal. The thermal conductivity $\kappa(T)$ of $CaCoO_3$ in Fig. 6(b) is low and glassy, which is contrary to that of metallic perovskites, such as $SrRuO_3$ [45] and $LaNiO_3$ [46].

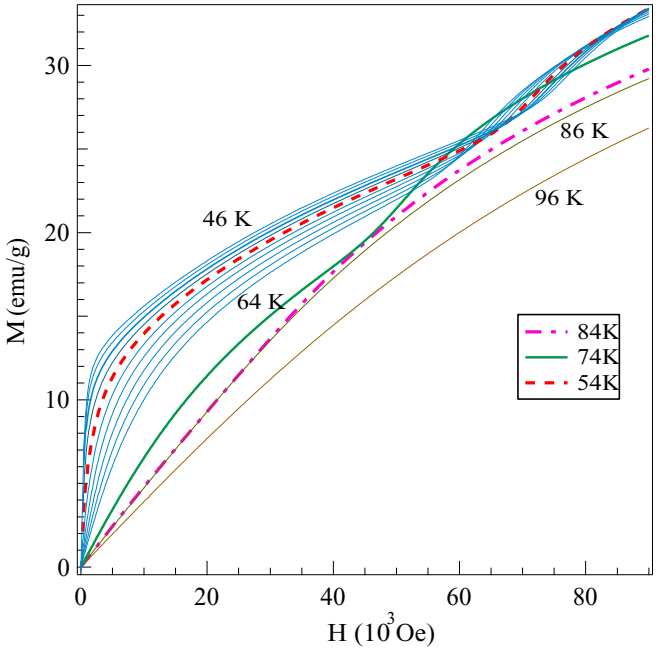

FIG. 3. The field dependence of the magnetization in a temperature range from 46 K to 64 K with $\Delta T = 2$ K. The $M(H)$ at $T_N \sim 86$ K and $T_C \sim 54$ K are highlighted by the dash-dotted lines.

As mentioned in the introduction, the spin-state transition from LS to HS in $RCoO_3$ is associated with an anomalously high thermal expansion. This observation motivated us to perform the structural study at different temperatures. The cubic phase remains stable to 20 K, the lowest temperature in the structural study. The temperature dependence of the Co-O bond length from the refinement of the XRD pattern is shown in Fig. 7 together with those of other perovskite oxides for comparison.

In the structural study under high pressure, we found that $CaCoO_3$ becomes unstable under high pressure; diffraction peaks become broad and new peaks not from the cubic phase

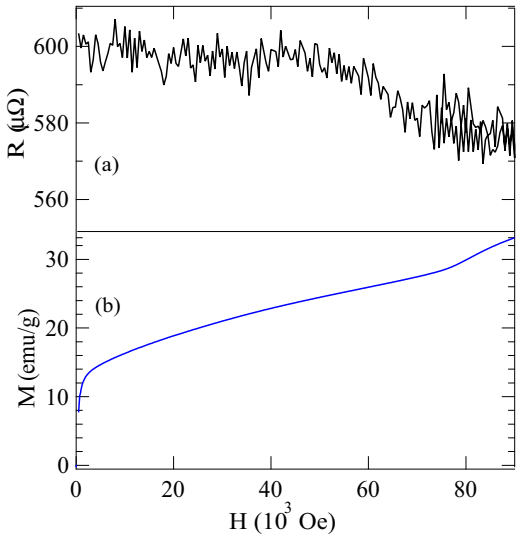

FIG. 4. The field dependence of (a) the magnetization and (b) the resistance for $CaCoO_3$ at 40 K.

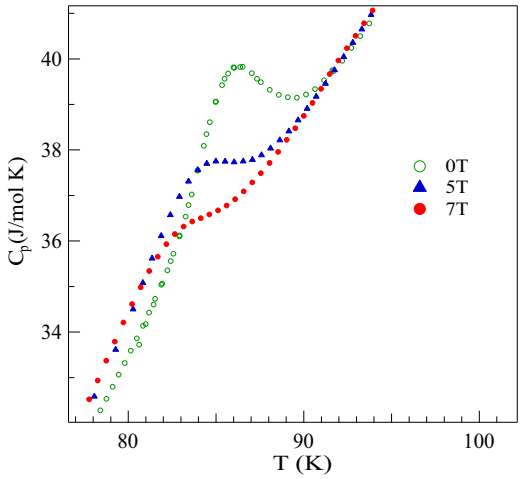

FIG. 5. The temperature dependence of specific heat for $CaCoO_3$ at different magnetic fields

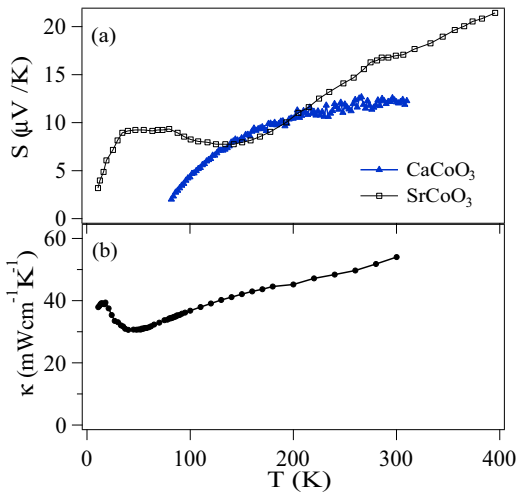

FIG. 6. Temperature dependence of (a) the thermoelectric power and (b) the thermal conductivity for $CaCoO_3$. The data of $SrCoO_3$ are after Ref. [30].

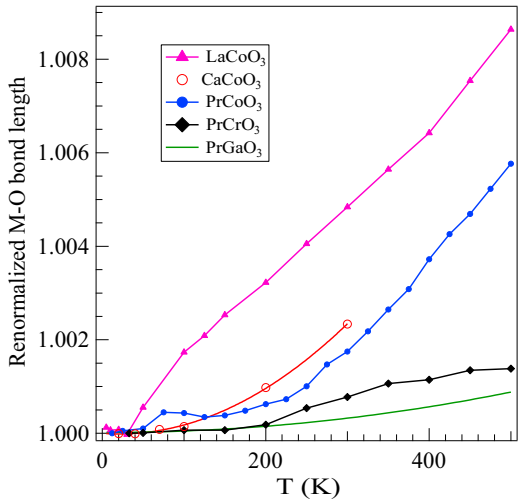

FIG. 7. Temperature dependence of renormalized M-O bond length of $CaCoO_3$ together with those of other perovskite oxides $CaMO_3$ for comparison.

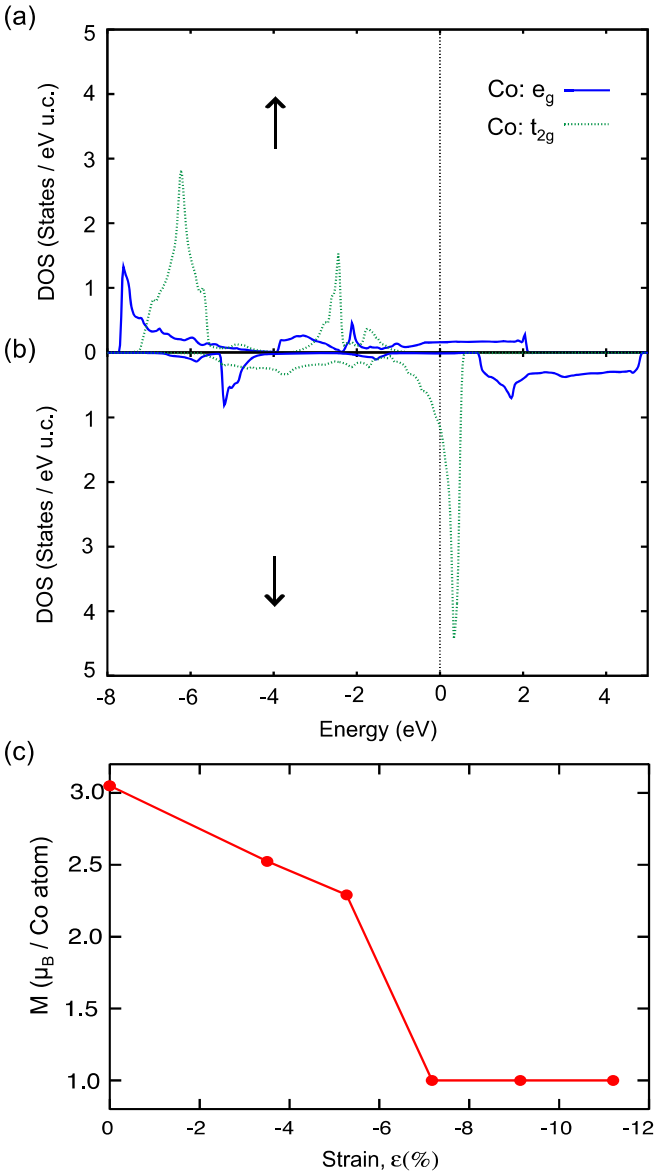

FIG. 8. Spin-polarized partial density of states of Co $3d$ for the cubic perovskite $CaCoO_3$ using GGA + U ($U = 4$ eV) with (a) spin-up, and (b) spin-down components. (c) Co magnetic moment as a function of isotropic lattice compression in $CaCoO_3$ in which $\varepsilon = (a/a_0 - 1) \times 100\%$.

appear. However, fitting the curve of V versus pressure at low pressures (to 2 GPa) in which the cubic phase component can still be identified, to the Birch-Murnaghan equation gives a bulk modulus $B_m = 165 \pm 8$ GPa. The B_m value is much smaller than that found in most perovskite oxides, but identical to that of $PrCoO_3$ where the unusually small B_m has been interpreted as a consequence of the pressure-induced spin-state transition from the HS to LS at room temperature [16].

Results of our GGA + U calculation of Figs. 8(a) and 8(b) and a previous DFT calculation [47] show that the Fermi energy cuts into both π^* and σ^* electron bands, which is consistent with the higher spin state. However, the calculated overlap between π^* and σ^* bands appears too large, which leads to a high saturation moment 2.4−3.0 μ_B close to that for

TABLE II. Structure and physical properties of $CaCoO_3$ and $SrCoO_3$. The theoretical calculation results of $SrCoO_3$ are after Ref. [47], whereas the results of $CaCoO_3$ are from this work.

		$SrCoO_3$	$CaCoO_3$
Space group	Theory	*Pm*-3*m*	*Pm*-3*m*
	Experiment	*Pm*-3*m*	*Pm*-3*m*
Lattice parameters/Co-O bond length (Å)	Theory	3.78/1.89	3.765/1.8825
	Experiment	3.83/1.915[a]	3.73431(6)/1.867
		3.83/1.915[b]	
Saturation moment (μ_B)	Theory	2.448 ($U = 0$)	2.396 ($U_{eff} = 0$ eV)
			2.791 ($U_{eff} = 3$ eV)
			3.050 ($U_{eff} = 4$ eV)
	Experiment	2.50	0.75[c]
μ_{eff} (μ_B)	Theory		
	Experiment		3.58
γ (mJ K^{-2} mol^{-1})	Theory	7.3	8.1 ($U_{eff} = 0$ eV)
			6.4 ($U_{eff} = 3$ eV)
			5.7 ($U_{eff} = 4$ eV)
	Experiment	45.7	53–71[d]
A (10^{-5} mΩ cm K^{-2})	Theory		
	Experiment	2–9	2.7[e]

[a]Data from Ref. [9].
[b]Data from Ref. [30].
[c]A continuous increase of the magnetization is due to the field-induced spin state transition; this is a cutoff value at $H = 4$ T.
[d]This value is sample dependent.
[e]Fitting to the Fermi-liquid behavior cannot be performed at very low temperature since there is an obvious resistivity downturn at $T <\sim 10$ K; this value was obtained from a fitting at $T > 10$ K.

the IS state. The lattice parameter is also slightly higher than the experimental value at 20 K. By reducing the cell parameter, our calculation successfully predicts a transition from the IS spin state to LS spin state as shown in Fig. 8(c).

IV. DISCUSSION

Physical properties of $CaCoO_3$ and $SrCoO_3$ are summarized in Table II together with the results from the electronic structure calculations for comparison. Co(IV) in the cubic $SrCoO_3$ is in the IS state; the paramagnetic susceptibility of $CaCoO_3$ suggests that $CaCoO_3$ is also in the IS state. The evolution of electrons in the π^* and σ^* band from $SrCoO_3$ to $CaCoO_3$ would be a key to understanding the peculiar transport and magnetic properties found in $CaCoO_3$. The change of electronic behavior is normally reflected in the crystal structure.

There is no doubt that electrons in the σ^* band of $SrCoO_3$ are itinerant. Ferromagnetism in the perovskite is mediated by the direct exchange interaction in a system with localized electrons on t_2 orbitals and itinerant electrons in the σ^* band. In contrast to all AMO_3 perovskites (A = Ca, Sr, Ba, M = transition metals, Ge, Sn, Zr) where the replacement of Sr by Ca always ends up with a cubic to orthorhombic transition and/or an enlarged octahedral-site rotation and M-O bond length in the *Pbnm* structure [39], the same chemical substitution in $ACoO_3$ does not lead to a change in the crystal

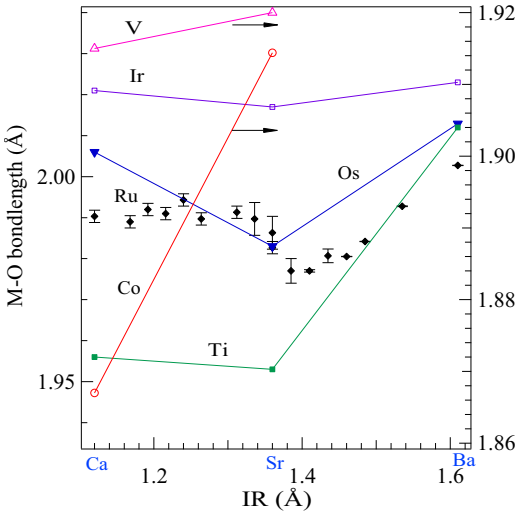

FIG. 9. The M-O bond length as a function of ionic radius (IR) of alkaline-earth element in perovskite oxides AMO_3.

symmetry, but to a collapse of the Co-O bond length within the cubic space group. The Co-O bond length in $ACoO_3$ versus the ionic radius (IR) of the A cation is plotted in Fig. 9 together with other transition-metal perovskites AMO_3 (M = Ti, V, Ru, Os, Ir) [40,48–56] for comparison. The metallic AVO_3 is the only other family to show a bond length contraction from $SrVO_3$ to $CaVO_3$. Electrons in the π^* band of these vanadate oxides are itinerant. However, the bond length contraction from $SrMO_3$ to $CaMO_3$ is much more dramatic in $ACoO_3$ than that in AVO_3, as is displayed. This change places $CaCoO_3$ to be the perovskite oxide having the smallest unit cell and M-O bond length in the literature so far. The most conducting perovskite ReO_3 has all the A sites vacant, but the M-O bond length (1.873 Å) in ReO_3 [57] is slightly larger than that in $CaCoO_3$. This structural analysis signals that electrons in both t_2 and e_g orbitals may be delocalized in $CaCoO_3$. If so, the low-temperature magnetic phases in $CaCoO_3$ should be attributed to itinerant electron magnetism.

Linear behavior in the Arrott plot of magnetization is a direct consequence of itinerant electron ferromagnetism [58]. For this test, we have converted the isothermal $M(H)$ of Fig. 3 into the Arrott plot in Fig. 10. The obvious anomaly at high fields is due to a field-induced transition; more discussion about the field-induced transition will be given in a following paragraph. The majority of the isothermal near T_c can be fitted by straight lines; the extension of the line corresponding to T_c passes through the origin. All Heisenberg magnets with localized moments would have all isotherms with concaved curvature in the Arrott plot. $SrRuO_3$ is the only perovskite oxide showing a straight line in the Arrott plot so far [59]. However, interpreting the observation as evidence of itinerant electron ferromagnetism in $SrRuO_3$ is not straightforward. Interested readers are referred to a previous study on this [60]. In another test for itinerant electron ferromagnetism, we have placed the magnetic properties of $CaCoO_3$ in a Rhodes-Wohlfarth (RW) plot of μ_{eff}/M_s versus T_c in Fig. 11. Existing ferromagnets are located on two wings in the RW plot;

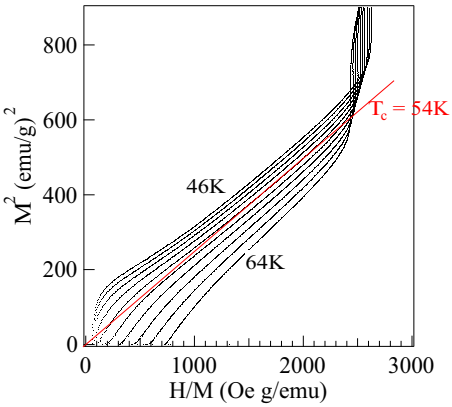

FIG. 10. The Arrott plot of isothermals for $CaCoO_3$ in the temperature range 46–64 K with $\Delta T = 2$ K.

those with itinerant electron magnetism are on the wing with a large μ_{eff}/M_s ratio and lower T_c, whereas those with localized moments are close to the line with a small μ_{eff}/M_s ratio and higher T_c [61]. $SrCoO_3$ becomes unstable at $T > T_c$, so that the μ_{eff} cannot be determined. Since the saturation moment of $SrCoO_3$ is consistent with that of the IS state of Co^{4+}, it would be a good assumption to take a $\mu_{\text{eff}} = 3.87\ \mu_B$ of the IS state for $SrCoO_3$. Therefore, a much higher T_c and a higher M_s make $SrCoO_3$ in line with localized moment ferromagnetism. In contrast, $CaCoO_3$ is close to the line of itinerant electron ferromagnetism. As a matter of fact, the spot of $CaCoO_3$ on the plot is near that for $ZrZn_2$, a prototype material for itinerant electron ferromagnetism.

While fitting the paramagnetic susceptibility of $CaCoO_3$ to a Curie-Weiss law gives a μ_{eff} that is close to the value for the IS state, the saturation moment at 2 K is even smaller than that for the LS state. In order to solve this puzzle, we have monitored the crystal structure of $CaCoO_3$ at low temperatures. The temperature dependence of the Co-O bond length (normalized to that at lowest temperature) is plotted in Fig. 7 together with other perovskite oxides for comparison [14]. We start from $PrGaO_3$ and $PrCrO_3$ in this analysis. $PrGaO_3$ serves as the base for the thermal expansion of the M-O bond length in a

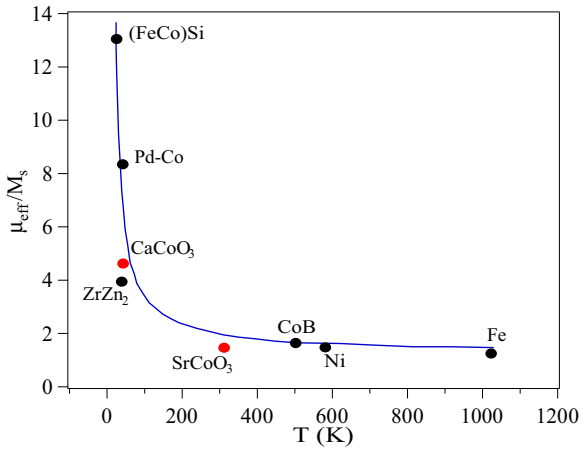

FIG. 11. The Rhodes-Wohlfarth plot of typical magnets; the data of magnets other than $SrCoO_3$ and $CaCoO_3$ are after Ref. [61].

perovskite oxide without any transitions associated with spin and charge [62]. $PrCrO_3$ behaves like $PrGaO_3$ except for a narrow temperature range near room temperature where the magnetorestriction associated with an antiferromagnetic spin ordering appears to alter the thermal expansion. In $LaCoO_3$ where the thermally driven spin-state transition from the LS to HS state starts at 25 K, a thermal expansion of the Co-O bond length that is much higher than that of either $PrGaO_3$ or $PrCrO_3$ has been reported [7]. In $PrCoO_3$, the onset temperature of the LS to HS transition moves to 200 K where an extra gain of the thermal expansion can be clearly seen [14]. The unusually high thermal expansion, especially at $T > 130$ K found in $CaCoO_3$, suggests continuous spin-state transition from the LS to the IS state, i.e., continuously pumping electrons from the π^* band to the σ^* band, as temperature increases. The scenario of a temperature-driven spin-state transition is also well supported by a low and glassy thermal conductivity found in $CaCoO_3$ displayed in Fig. 6(b) since the thermally driven spin-state change is associated with bond-length fluctuations. A similar thermal conductivity has been reported in $LaCoO_3$ and $PrCoO_3$ [10]. The LS state is stabilized below room temperature in $NdCoO_3$ where the phonon thermal conductivity is restored [10]. The observation of a thermally driven spin-state transition also implies that the electronic states in the π^* band and σ^* band are nearly degenerate in $CaCoO_3$, which opens the possibility of a field-induced spin-state transition.

Figure 12 illustrates a schematic diagram of the spin state and the band structure of $CaCoO_3$. The IS state can be defined from the free-ion model with a cubic field on the left. The Co-O bonding in the perovskite structure transforms the localized orbital energies into bonding and antibonding bands; the Fermi energy is located inside and antibonding π^* and σ^* bands are shown in the middle. The exchange splitting in the ferromagnetic phase shifts the band of up-spin relative to that of down-spin. The net moment is $M = \mu_B(n_{\pi\uparrow} + n_{\sigma\uparrow} - n_{\pi\downarrow})$ that is parallel to the external field for a $H > H_c$ (the coercive field of the magnet). Therefore, the effect of an external field is to further stabilize the up-spin bands relative to the down-spin bands. This field-induced band shift will lead to transferring electrons from the $\pi^*(\downarrow)$ band to $\sigma^*(\uparrow)$. The field-induced metamagnetic transition to the state with higher magnetization shown in Fig. 2(d) and Fig. 3 supports the argument very well. Since the σ^* bandwidth is broader than that of the π^* band, the magnetization increase should be coupled with a gain of the conductivity, which is consistent with the observation in Fig. 4. The field-induced electron transfer from the π^* to σ^* band is also the origin of a giant negative magnetoresistance shown in Fig. 2(f).

A clear deviation from a Curie-Weiss law fitting in the inverse magnetic susceptibility in Fig. 2(a) can be found near 150 K. Moreover, a nonlinear magnetization curve $M(H)$ indicates that magnetic fluctuations take place below 150 K. A remarkable change of $M(H)$ on cooling through T_N is that the magnetic field induces an obvious transition at $H_T \sim 5$ T in the $M(H)$ isothermals below T_N, as illustrated in Fig. 3. This field-induced transition moves to a higher field as temperature further decreases from T_N. There is no noticeable change of the $M(H)$ curve on cooling through T_c. We may look for a clue to explain these anomalous magnetic properties from the

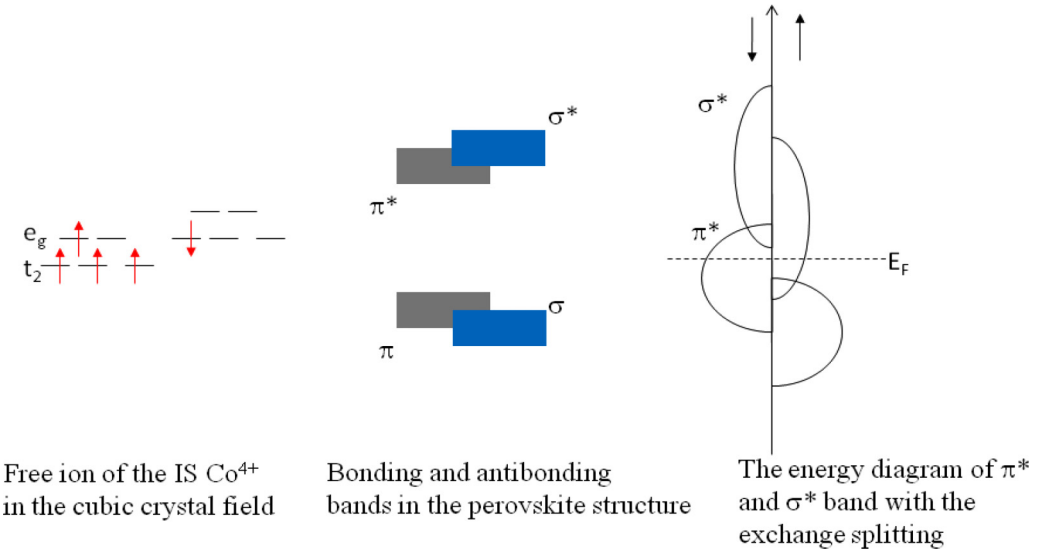

FIG. 12. The schematic energy diagram of the IS state for $CaCoO_3$.

structural data. Although there is no structural transition on cooling through these magnetic transitions, the temperature dependence of Co-O bond length undergoes a major change at $T \sim 100$ K, as shown in Fig. 7. A negligible thermal expansion of Co-O bond length below 100 K suggests that $CaCoO_3$ has predominately the LS state at $T < T_N$, whereas an unusually high thermal expansion coefficient of the Co-O bond length at $T > T_N$ means a continuous increase of the IS state as temperature increases. The LS state at low temperatures is consistent with the saturation moment $M_s < 1\ \mu_B$ observed and the HS state at high temperatures is close to the μ_{eff} extracted from the paramagnetic susceptibility. Therefore, T_N actually marks an onset temperature for the spin-state transition in addition to ordering spins into an AF structure. The AF spin structure evolves into a ferromagnetic phase (perhaps still with some spiral-spin component) on cooling through T_c. In the magnetically ordered phases either below T_N or T_c, the peculiar band structure in $CaCoO_3$ where the Fermi energy cuts into both degenerate $\pi^*(\downarrow)$ and $\sigma^*(\uparrow)$ makes it possible that a magnetic field induces a transition from the LS state to the higher spin state.

One may be curious about (1) whether the Curie-Weiss law remains valid for $CaCoO_3$ which is now identified as exhibiting itinerant electron magnetism and (2) μ_{eff} and M_s in the RW plot have been measured at temperatures where different spin states have been identified. The temperature dependence of magnetic susceptibility for $ZrZn_2$ can be fitted by the Curie-Weiss law almost perfectly at $T > 100$ K [63]. The Curie constant from the fitting can be generally expressed as $C = gq$. Although the q value is not far from $[S(S+1)]^{1/2}$ for localized spins, it is actually related to the electronic density of state (EOS) at the Fermi energy as derived from the unified picture of magnetism by Moriya [64]. Since the Curie constant C is related to the EOS of itinerant electrons in $CaCoO_3$, the spin-state change in the band picture may not induce a change in the C value as much as that for a localized spin system. Moreover, the spin-state transition from the LS to the IS state at $T > T_N$ is progressive. The dramatic difference of the RW ratio C/M_s between $CaCoO_3$ and $SrCoO_3$ is actually dominated by the change of the saturation moment M_s.

The electronic contribution to specific heat C_p has been obtained by fitting the $C_p(T)$ data in Fig. 2(b) to the formula $C_p = \gamma T + \alpha T^{3/2} + \beta T^3$ at low temperatures. A $\gamma = 53$ mJ K^{-2} mol^{-1} is significantly higher than the $\gamma_0 =$ 5.7–8.1 mJ K^{-2} mol^{-1} from the band structural calculation in this work and from the literature [47]; this γ value is also higher than those of typical $\sigma*$ band metals like $LaNiO_3$ ($\gamma =$ 18.1 mJ K^{-2} mol^{-1}) and $LaCuO_3$ ($\gamma = 5.6$ mJ K^{-2} mol^{-1}) [65]. The only possibility for $CaCoO_3$ to have such a high γ is that the highly correlated π^* electrons which facilitate ferromagnetism also contribute to the specific-heat and transport properties. A similar $\gamma = 45$ mJ K^{-2} mol^{-1} has also been obtained for the isostructural $SrCoO_3$. The unusually high γ value of $CaCoO_3$ is rarely observed in $3d$ oxides. We have performed dynamical mean-field calculations to take into account possible Kondo hybridization, but found no evidence of enhanced renormalization of band structures from a strongly correlation effect. The Van Hove singularity is too far away from the Fermi energy to yield a large γ. Thus the heavy-fermion behavior in $CaCoO_3$ remains a mystery as in the case of LiV_2O_4 [66,67] and demands further investigation. Although $CaCoO_3$ has the highest γ value of the simple metallic perovskites, the ratio γ^2/A is not far from the Kadowaki-Woods ratio $\gamma^2/A = 1/a_0 \sim 10^{11}$ (mJ^2 K^{-2} mol^{-2} cm^{-2} Ω^{-2}) [68], where A is a coefficient of the formula $\rho = \rho_0 + AT^2$ used to fit the temperature dependence of resistivity at low temperatures.

In conclusion, a new perovskite oxide $CaCoO_3$ has been synthesized by treating the brownmillerite-type precursor $Ca_2Co_2O_5$ under high pressure and high temperature. $CaCoO_3$ is the first $CaMO_3$ (M = transition metal, Ge, Sn, and Zr) perovskite reported which is cubic at room temperature. Like the perovskites with Co(III) such as $LaCoO_3$ and $PrCoO_3$ at room temperature, both $SrCoO_3$ and $CaCoO_3$ have the down-

spin t_2 energies close to the up-spin e_g energies. The metallic conductivity down to 1.8 K in these perovskites with Co(IV) indicates that the σ^* electrons are itinerant. Furthermore, the Co-O bond length in $CaCoO_3$ is the shortest in all transition-metal perovskites and promises that t_2 electrons are itinerant. Itinerant electron ferromagnetism below $T_c \approx 54$ K can be well supported by (a) nearly linear isothermal near in the vicinity of T_c in an Arrott plot and (2) the location of $CaCoO_3$ which is near that of $ZrZn_2$ in the Rhodes-Wohlfarth plot of the magnetic properties. In contrast, $SrCoO_3$ is located in a regime typical for localized magnetism in this plot. In $CaCoO_3$, spins are ordered into an AF structure below $T_N \approx 86$ K and further evolve into a ferromagnetic state below T_c. The magnetic ordering transition at T_N also separates the spin state below T_N that is dominated by the LS state from the high-temperature phase showing a thermally driven LS-HS transition at $T > T_N$. The peculiar band structure of $CaCoO_3$ makes it possible that magnetic field induces the LS to HS transition in the phase below T_N and T_c.

ACKNOWLEDGMENTS

The authors are grateful to Q. F. Zhang, Z. G. Sheng, and J. Q. Yan for enlightening discussion and to J. B. Goodenough for reviewing and commenting on the manuscript. This work was supported by the 973 Project of the Ministry of Science and Technology of China (Grant No. 2014CB921500), the Strategic Priority Research Program of the Chinese Academy of Sciences (Grant No. XDB07030300), and the National Natural Science Foundation of China (Grant No. 11574378). J.S.Z. was supported by DOD-ARMY (W911NF-16-1-0559). M.A.M. acknowledges support from the US Department of Energy, Office of Science, Basic Energy Sciences, Materials Sciences and Engineering Division.

[1] J. B. Goodenough, J. Phys. Chem. Solids **6**, 287 (1958).
[2] P. M. Raccah and J. B. Goodenough, Phys. Rev. **155**, 932 (1967).
[3] M. A. Señaris-Rodriguez and J. B. Goodenough, J. Solid State Chem. **118**, 323 (1995).
[4] M. A. Señaris-Rodriguez and J. B. Goodenough, J. Solid State Chem. **116**, 224 (1995).
[5] C. Zobel, M. Kriener, D. Bruns, J. Baier, M. Grüninger, T. Lorenz, P. Reutler, and A. Revcolevschi, Phys. Rev. B **71**, 019902 (2005).
[6] J. Baier, S. Jodlauk, M. Kriener, A. Reichl, C. Zobel, H. Kierspel, A. Freimuth, and T. Lorenz, Phys. Rev. B **71**, 014443 (2005).
[7] P. G. Radaelli and S. W. Cheong, Phys. Rev. B **66**, 094408 (2002).
[8] R. H. Potze, G. A. Sawatzky, and M. Abbate, Phys. Rev. B **51**, 11501 (1995).
[9] Y. W. Long, Y. Kaneko, S. Ishiwata, Y. Taguchi, and Y. Tokura, J. Phys.: Condens. Matter **23**, 245601 (2011).
[10] J. Q. Yan, J. S. Zhou, and J. B. Goodenough, Phys. Rev. B **69**, 134409 (2004).
[11] S. Yamaguchi, Y. Okimoto, and Y. Tokura, Phys. Rev. B **54**, R11022 (1996).
[12] V. Oygarden, H. L. Lein, and T. Grande, J. Solid State Chem. **192**, 246 (2012).
[13] V. Oygarden and T. Grande, Dalton Trans. **42**, 2704 (2013).
[14] Y. Ren, J.-Q. Yan, J.-S. Zhou, J. B. Goodenough, J. D. Jorgensen, S. Short, H. Kim, Th. Proffen, S. Chang, and R. J. McQueeney, Phys. Rev. B **84**, 214409 (2011).
[15] T. Vogt, J. A. Hriljac, N. C. Hyatt, and P. Woodward, Phys. Rev. B **67**, 140401 (2003).
[16] J. S. Zhou, J. Q. Yan, and J. B. Goodenough, Phys. Rev. B **71**, 220103 (2005).
[17] S. Y. Fu, J. Yang, and J. F. Lin, Phys. Rev. Lett. **118**, 036402 (2017).
[18] J. Suntivich, K. J. May, H. A. Gasteiger, J. B. Goodenough, and Y. Shao-Horn, Science **334**, 1383 (2011).
[19] P. Lacorre, J. B. Torrance, J. Pannetier, A. I. Nazzal, P. W. Wang, and T. C. Huang, J. Solid State Chem. **91**, 225 (1991).
[20] J. B. Torrance, P. Lacorre, A. I. Nazzal, E. J. Ansaldo, and C. Niedermayer, Phys. Rev. B **45**, 8209 (1992).
[21] J. L. Garcia-Muñoz, J. Rodriguez-Carvajal, P. Lacorre, and J. B. Torrance, Phys. Rev. B **46**, 4414 (1992).
[22] X. Obradors, L. M. Paulius, M. B. Maple, J. B. Torrance, A. I. Nazzal, J. Fontcuberta, and X. Granados, Phys. Rev. B **47**, 12353 (1993).
[23] P. C. Canfield, J. D. Thompson, S. W. Cheong, and L. W. Rupp, Phys. Rev. B **47**, 12357 (1993).
[24] J. S. Zhou, J. B. Goodenough, B. Dabrowski, P. W. Klamut, and Z. Bukowski, Phys. Rev. B **61**, 4401 (2000).
[25] J. S. Zhou and J. B. Goodenough, Phys. Rev. B **69**, 153105 (2004).
[26] M. J. Rozenberg, G. Kotliar, and X. Y. Zhang, Phys. Rev. B **49**, 10181 (1994).
[27] E. E. Rodriguez, F. Poineau, A. Llobet, B. J. Kennedy, M. Avdeev, G. J. Thorogood, M. L. Carter, R. Seshadri, D. J. Singh, and A. K. Cheetham, Phys. Rev. Lett. **106**, 067201 (2011).
[28] M. Avdeev, G. J. Thorogood, M. L. Carter, B. J. Kennedy, J. Ting, D. J. Singh, and K. S. Wallwork, J. Am. Chem. Soc. **133**, 1654 (2011).
[29] V. S. Borisov, I. V. Maznichenko, D. Bottcher, S. Ostanin, A. Ernst, J. Henk, and I. Mertig, Phys. Rev. B **85**, 134410 (2012).
[30] S. Balamurugan, K. Yamaura, A. B. Karki, D. P. Young, M. Arai, and E. Takayama-Muromachi, Phys. Rev. B **74**, 172406 (2006).
[31] M. W. Lufaso and P. M. Woodward, Acta Crystallogr. B **57**, 725 (2001).
[32] Y. W. Long, Y. Kaneko, S. Ishiwata, Y. Tokunaga, T. Matsuda, H. Wadati, Y. Tanaka, S. Shin, Y. Tokura, and Y. Taguchi, Phys. Rev. B **86**, 064436 (2012).
[33] J. J. Zhang, H. Zheng, C. D. Malliakas, J. M. Allred, Y. Ren, Q. A. Li, T. H. Han, and J. F. Mitchell, Chem. Mater. **26**, 7172 (2014).
[34] Y. W. Long, T. Saito, T. Tohyama, K. Oka, M. Azuma, and Y. Shimakawa, Inorg. Chem. **48**, 8489 (2009).
[35] J. Rodriguez-Carvajal, Physica B **192**, 55 (1993).
[36] P. Blaha, K. Schwarz, P. Sorantin, and S. B. Trickey, Comput. Phys. Commun. **59**, 399 (1990).

[37] P. Blaha, K. Schwarz, G. K. H. Madsen, D. Kvasnicka, and J. Luitz, *WIEN2k: An Augmented Plane Wave + Local Orbitals Program for Calculating Crystal Properties* (Karlheinz Schwarz, Technische Universitat Wien, 2014).
[38] J. P. Perdew, K. Burke, and M. Ernzerhof, Phys. Rev. Lett. **77**, 3865 (1996).
[39] J. B. Goodenough and J. M. Longo, Crystallographic and magnetic properties of perovskite and perovskite-related compounds, in *Magnetic and Other Properties of Oxides and Related Compounds*, Landolt-Börnstein, New Series, Group III, Vol. 4, Pt. A (Springer-Verlag, Berlin, 1970).
[40] R. Ali and M. Yashima, J. Solid State Chem. **178**, 2867 (2005).
[41] M. Yashima and R. Ali, Solid State Ionics **180**, 120 (2009).
[42] G. Cao, S. McCall, M. Shepard, J. E. Crow, and R. P. Guertin, Phys. Rev. B **56**, 321 (1997).
[43] P. B. Allen, H. Berger, O. Chauvet, L. Forro, T. Jarlborg, A. Junod, B. Revaz, and G. Santi, Phys. Rev. B **53**, 4393 (1996).
[44] R. J. Bouchard and J. L. Gillson, Mater. Res. Bull. **7**, 873 (1972).
[45] M. Shepard, P. F. Henning, G. Cao, and J. E. Crow, J. Appl. Phys. **83**, 6989 (1998).
[46] J. S. Zhou, J. B. Goodenough, and B. Dabrowski, Phys. Rev. B **67**, 020404 (2003).
[47] Z. Ali and I. Ahmad, J. Electron. Mater. **42**, 438 (2013).
[48] G. B. Li, X. J. Kuang, S. J. Tian, F. H. Liao, X. P. Jing, Y. Uesu, and K. Kohn, J. Solid State Chem. **165**, 381 (2002).
[49] H. T. Evans, Acta Crystallogr. **4**, 377 (1951).
[50] G. H. Kwei, A. C. Lawson, S. J. L. Billinge, and S. W. Cheong, J. Phys. Chem. **97**, 2368 (1993).
[51] J. Garcia-Jaca, J. I. R. Larramendi, M. Insausti, M. I. Arriortua, and T. Rojo, J. Mater. Chem. **5**, 1995 (1995).
[52] J. Garcia-Jaca, J. L. Mesa, M. Insausti, J. I. R. Larramendi, M. I. Arriortua, and T. Rojo, Mater. Res. Bull. **34**, 289 (1999).
[53] J. G. Cheng, J. S. Zhou, and J. B. Goodenough, Proc. Natl. Acad. Sci. U.S.A. **110**, 13312 (2013).
[54] Y. G. Shi *et al.*, J. Am. Chem. Soc. **135**, 16507 (2013).
[55] J. G. Cheng, J. S. Zhou, J. B. Goodenough, Y. Sui, Y. Ren, and M. R. Suchomel, Phys. Rev. B **83**, 064401 (2011).
[56] P. E. R. Blanchard, E. Reynolds, B. J. Kennedy, J. A. Kimpton, M. Avdeev, and A. A. Belik, Phys. Rev. B **89**, 214106 (2014).
[57] T. Chatterji, P. F. Henry, R. Mittal, and S. L. Chaplot, Phys. Rev. B **78**, 134105 (2008).
[58] E. P. Wohlfarth, J. Appl. Phys. **39**, 1061 (1968).
[59] D. Kim, B. L. Zink, F. Hellman, S. McCall, G. Cao, and J. E. Crow, Phys. Rev. B **67**, 100406(R) (2003).
[60] J. G. Cheng, J. S. Zhou, J. B. Goodenough, and C. Q. Jin, Phys. Rev. B **85**, 184430 (2012).
[61] P. Mohn, *Magnetism in the Solid State: An Introduction* (Springer, Berlin, 2006).
[62] L. Vasylechko, Y. Pivak, A. Senyshyn, D. Savytskii, M. Berkowski, H. Borrmann, M. Knapp, and C. Paulmann, J. Solid State Chem. **178**, 270 (2005).
[63] S. Ogawa and N. Sakamoto, J. Phys. Soc. Jpn. **22**, 1214 (1967).
[64] T. Moriya, *Electron Correlation and Magnetism in Narrow-Band Systems* (Springer-Verlag, Berlin, 1981).
[65] J. S. Zhou, L. G. Marshall, and J. B. Goodenough, Phys. Rev. B **89**, 245138 (2014).
[66] S. Kondo, D. C. Johnston, C. A. Swenson, F. Borsa, A. V. Mahajan, L. L. Miller, T. Gu, A. I. Goldman, M. B. Maple, D. A. Gajewski, E. J. Freeman, N. R. Dilley, R. P. Dickey, J. Merrin, K. Kojima, G. M. Luke, Y. J. Uemura, O. Chmaissem, and J. D. Jorgensen, Phys. Rev. Lett. **78**, 3729 (1997).
[67] C. Urano, M. Nohara, S. Kondo, F. Sakai, H. Takagi, T. Shiraki, and T. Okubo, Phys. Rev. Lett. **85**, 1052 (2000).
[68] N. E. Hussey, J. Phys. Soc. Jpn. **74**, 1107 (2005).
[69] See Supplemental Material at http://link.aps.org/supplemental/10.1103/PhysRevMaterials.1.024406 for the refinement of X-ray diffraction pattern with different structural models.